OPTICA

Transport-of-intensity Fourier ptychographic diffraction tomography: defying the matched illumination condition

Shun Zhou,[1,2,3,†] Jiaji Li,[1,2,3,†] Jiasong Sun,[1,2,3] Ning Zhou,[1,2,3] Habib Ullah,[1,2,3] Zhidong Bai,[1,2,3] Qian Chen,[1,3,4] and Chao Zuo[1,2,3,5]

[1]Smart Computational Imaging Laboratory (SCILab), School of Electronic and Optical Engineering, Nanjing University of Science and Technology, Nanjing, Jiangsu Province 210094, China
[2]Smart Computational Imaging Research Institute (SCIRI) of Nanjing University of Science and Technology, Nanjing, Jiangsu Province 210019, China
[3]Jiangsu Key Laboratory of Spectral Imaging & Intelligent Sense, Nanjing, Jiangsu Province 210094, China
[4]e-mail: chenqian@njust.edu.cn
[5]e-mail: zuochao@njust.edu.cn

Received 23 September 2022; revised 20 October 2022; accepted 25 October 2022; published 8 December 2022

Optical diffraction tomography (ODT) is a promising label-free three-dimensional (3D) microscopic method capable of measuring the 3D refractive index (RI) distribution of optically transparent samples (e.g., unlabeled biological cells). In recent years, non-interferometric ODT techniques have received increasing attention for their system simplicity, speckle-free imaging quality, and compatibility with existing microscopes. However, ODT methods for implementing non-interferometric measurements in high numerical aperture (NA) microscopy systems are often plagued by low-frequency missing problems—a consequence of violating the matched illumination condition. Here, we present transport-of-intensity Fourier ptychographic diffraction tomography (TI-FPDT) to address this challenging issue by combining ptychographic angular diversity with additional "transport of intensity" measurements. TI-FPDT exploits the defocused phase contrast to circumvent the stringent requirement on the illumination NA imposed by the matched illumination condition. It effectively overcomes the reconstruction quality deterioration and RI underestimation problems in conventional FPDT, as demonstrated by high-resolution tomographic imaging of various unlabeled transparent samples (including microspheres, USAF targets, HeLa cells, and C2C12 cells). Due to its simplicity and effectiveness, TI-FPDT is anticipated to open new possibilities for label-free 3D microscopy in various biomedical applications.

https://doi.org/10.1364/OPTICA.476474

1. INTRODUCTION

Optical diffraction tomography (ODT) exploits the refractive index (RI) as the intrinsic optical imaging contrast to visualize or quantitatively characterize cellular features, which has shown practical value in biological research, medical diagnosis, and drug discovery [1–6]. Over the past decades, various types of ODT techniques [7–12] have been developed to infer the volumetric RI distribution of biological samples by combining optical holography [13,14] with computed tomography [15], enabling non-invasive and label-free three-dimensional (3D) volumetric imaging of transparent samples. These typical coherent ODT techniques, either for object rotation or illumination scanning, essentially perform the process of coherent synthetic aperture [8,16–18], which accesses the different spatial frequency information through the relative angular changes between the sample and the illumination beams. And further, all acquired frequency components in 3D Fourier space are synthesized together to get the scattering potential for characterizing the RI of the object. By involving interferometric or holographic measurements, the complex amplitude distribution of the total field can be obtained directly in conventional ODT systems [7] (e.g., Mach–Zehnder interferometers equipped with galvanometer scanning mirrors), and further the first-order scattered field can be determined according to Born/Rytov approximations [9,19,20].

Under the framework of Fourier diffraction theorem [19,21], the two-dimensional (2D) spectrum of the first-order scattered field is directly related to the object's 3D frequency content within a generalized aperture defined as the projection of the 2D complex pupil function onto the 3D Ewald sphere. For each coherent illumination, the frequency information corresponding to the support of the 3D Ewald sphere is transferred with maximum contrast due to the unit amplitude response of the coherent transfer function. Unfortunately, because of the use of temporally coherent illumination, these coherent ODT techniques suffer from inevitable speckle noise and parasitic interference, preventing high-quality 3D RI imaging [22]. Moreover, most of them require specialized interferometric setups with complicated beam scanning or sample rotation devices, prohibiting their widespread application in the

biological and medical communities. To fundamentally overcome these limitations, the ODT in non-interferometric manners seeks to recover the RI distribution of samples from the intensity-only measurement, and the related non-interferometric 3D label-free technique has also been a hot research topic recently [23–29].

Similar to the typical ODT techniques, asymmetric-illumination-based non-interferometric diffraction tomography also relies on the relative angular changes between the sample and the illumination beams, and the 2D intensity images under diverse illumination are acquired for 3D object scattering reconstruction. However, the spectrum information located on the Ewald sphere is unavailable directly due to the loss of phase component in the complex amplitude field for intensity recording. Thus, it is crucial to recover the required scattered field (including both amplitude and phase) of objects from the intensity measurement in non-interferometric ODT. For a partially coherent illumination imaging system, influenced by the degradation of illumination coherence and inherent intensity-only measurement, the frequency spectrum of intensity is determined by the system's phase transfer function (PTF). Different from the case of coherent illumination, the distribution of the transfer function value of corresponding partially coherent source is non-idealized (non-uniform frequency response) instead of unit amplitude response. Especially, the low-frequency phase components cannot be effectively transferred into the intensity measurement as a result of PTF overlap and cancellation around the zero-frequency point. For the case of the tilted incident illumination wave, the PTF associated with the intensity image contains two shifted anti-symmetric pupils that cancel each other out in the low-frequency region. Only if the illumination angle matches the numerical aperture (NA) of the objective lens (i.e., called matched illumination condition) will the two shifted pupils be tangent to each other, and there will be no more overlap in the low-frequency region, thus allowing complete transfer of low-frequency phase components to the intensity image [30]. However, it is difficult to strictly fulfill the matched illumination condition in experiments, especially for high-NA imaging systems. Failure to meet the matched illumination condition precludes the intact recovery of the phase component due to the low-frequency spectral overlapping in the captured intensity, bringing a daunting challenge to asymmetric-illumination-based non-interferometric diffraction tomography with high-NA objectives.

We recently found that two 2D anti-symmetrical pupils of the PTF will become back-to-back 3D generalized apertures by extending the intensity measurement into 3D space, and that the distribution of these 3D apertures in the Fourier space are pass-band filter sphere caps and no longer cancel each other out under arbitrary illumination angles [31]. The total separation of two independent generalized apertures (overlapped at zero point) eliminates the requirement of the matched illumination condition, and the 3D scattering potential can be reconstructed under arbitrary illumination conditions similar to the case of holographic diffraction tomography. Nevertheless, the data requirement of previous work is about 2 orders of magnitude larger than that of typical holographic diffraction tomography due to the introduction of additional axial scanning under each illumination angle, resulting in excessively time-consuming data acquisition and a severe burden on storage. And until now, asymmetric-illumination-based non-interference diffraction tomography has not been efficiently implemented in high-NA imaging systems to meet the urgent need for high-resolution, time-efficient, and small data volume biological imaging due to these limitations. In fact, only fewer intensity images are required to retrieve the lost phase information by using the transport of intensity equation (TIE) [32] under a certain illumination angle. Once the phase information is available, the 3D intensity stack needed to be measured in the previous work is highly redundant since it can be obtained by propagating a 2D complex amplitude into 3D space.

In this work, we present an effective solution to the challenging issue of the matched illumination condition by combining ptychographic iteration under angle-varied illumination [25,33] with additional "transport of intensity" measurements [34,35]. The proposed method, termed transport-of-intensity Fourier ptychographic diffraction tomography (TI-FPDT), retrieves the 3D RI distribution of the sample from two intensity sets containing images at two different focus positions under diverse illumination. Thanks to the significant low-frequency phase contrast provided by the additional defocused intensity images acquired at each illumination angle, TI-FPDT circumvents the stringent requirement on the illumination NA imposed by the matched illumination condition. As a result, this endows TI-FPDT with the capability to effectively overcome the reconstruction quality deterioration and RI underestimation problems in conventional FPDT under the non-matched illumination condition. Unlike typical ODT, TI-FPDT incorporates both in-focus and defocused intensity images in the FPDT framework and uses them as the constraint condition to recover the RI distribution of the sample and refine the reconstruction result, allowing for a more precise high-resolution tomographic imaging. Based on an off-the-shelf bright-field microscope equipped with a programmable light-emitting diode (LED) array as the light source, we realize high-resolution (327 nm/254 nm lateral resolution with dry/oil-immersion objectives, respectively) non-interferometric 3D RI reconstruction. The experimental results of polystyrene microspheres are consistent with the simulation, validating the ability of TI-FPDT to recover low-frequency components under the non-matched illumination condition. We further demonstrate the validity of TI-FPDT for imaging biological samples by high-resolution RI tomographic imaging and quantitative characterizations of unstained HeLa cells and C2C12 cells, suggesting that TI-FPDT is a promising tool for revealing organelle structures at the subcellular level. Due to its simplicity and effectiveness, the proposed TI-FPDT approach is expected to bypass the matched illumination barrier and open new possibilities for non-interferometric high-resolution ODT in various biological and medical applications.

2. PRINCIPLE

A. TI-FPDT Forward Imaging Model

In the basic theory of diffraction tomography, the physical quantity of interest to be retrieved is the scattering potential of a thick 3D sample, via the following expression:

$$O(\mathbf{x}) = k_0^2\left[n(\mathbf{x})^2 - n_m^2\right], \tag{1}$$

where $k_0 = 2\pi/\lambda$ is the wavenumber, with λ being the illumination wavelength in free space, while $n(\mathbf{x})$ and n_m are the spatial RI distribution of the sample and its surrounding medium, correspondingly. $\mathbf{x} = (\mathbf{x}_T, z) = (x, y, z)$ is a short-hand notation for the 3D spatial coordinate.

In the case where the 3D sample is illuminated by a plane wave $U_{\text{in}}(\mathbf{x})$, the resultant total field $U(\mathbf{x})$ is written as the superposition of the incident field $U_{\text{in}}(\mathbf{x})$ and the scattered field $U_s(\mathbf{x})$ (i.e., $U(\mathbf{x}) = U_{\text{in}}(\mathbf{x}) + U_s(\mathbf{x})$), which obeys the inhomogeneous wave equation. To obtain the analytical solution to the inverse scattering problem, we need to consider the single scattering events (first-order scattered field $U_{s1}(\mathbf{x})$), excluding multiple scattering. Further, the following relation known as the Fourier diffraction theorem [19] is obtained by employing Green's function [36], and then the first-order scattered field $U_{s1}(\mathbf{x}_T)$ can be related to the scattering potential $O(\mathbf{x})$ in 3D Fourier space:

$$\hat{O}(\mathbf{u}-\mathbf{u}_{\text{in}}) = 4\pi j u_z \exp(-2\pi j u_z z_D)\hat{U}_{s1}(\mathbf{u}_T;\, z=z_D) \times P(\mathbf{u}_T)\delta\left(u_z - \sqrt{u_m^2 - |\mathbf{u}_T|^2}\right), \tag{2}$$

where $\mathbf{u} = (\mathbf{u}_T, u_z) = (u_x, u_y, u_z)$ represents the 3D spatial frequency coordinates corresponding to $\mathbf{x}$ and $\mathbf{u}_{\text{in}} = (\mathbf{u}_{\text{in}T}, u_{\text{in}z}) = (u_{\text{in}x}, u_{\text{in}y}, u_{\text{in}z})$ is the 3D incident plane wave vector, while j is the imaginary unit and $u_m = n_m/\lambda$ is the spatial frequency in the medium n_m. $\hat{O}(\mathbf{u})$ and $\hat{U}_{s1}(\mathbf{u}_T)$ correspond to the 3D and 2D Fourier transforms of $O(\mathbf{x})$ and $U_{s1}(\mathbf{x}_T)$, respectively. $P(\mathbf{u}_T)\delta(u_z - \sqrt{u_m^2 - |\mathbf{u}_T|^2})$ is defined as the 3D coherent transfer function, whose spectrum support domain is a restricted Ewald sphere limited by the objective aperture. z_D represents the coordinate displacement in the z direction, i.e., the measurement is performed at different focus positions.

According to Eq. (2), it can be found that the information in the scattering potential spectrum corresponding to the Ewald support domain contains all the information of the 3D first-order scattering field $\hat{U}_{s1}(\mathbf{u})$ for a certain illumination angle [37]. More simply, there is an exponential factor correlation between the 2D first-order scattered fields at different axial positions in Fourier space, i.e.,

$$\hat{U}_{s1}(\mathbf{u}_T;\, z=\Delta z) = \exp(2\pi j u_z \Delta z)\hat{U}_{s1}(\mathbf{u}_T;\, z=0). \tag{3}$$

Since intensity-only images are utilized to realize RI tomographic imaging, the relationship between measured intensity images and the scattering potential of samples should be established. Considering better applicability of the Rytov approximation for imaging thick biological samples compared to the Born approximation [9,19,20], we choose the former one as the approximation implementation in this work (see Section 1 in Supplement 1 for detailed analysis). As a result, the relationship between the first-order scattered field and the measured intensity can be established as

$$\begin{cases} I(\mathbf{x}_T,\, z=0) = \left|U_{\text{in}} \exp\left[\frac{U_{s1}(\mathbf{x}_T, z=0)}{U_{\text{in}}}\right]\right|^2 & \text{In}-\text{focus}, \\ I(\mathbf{x}_T,\, z=\Delta z) = \left|U_{\text{in}} \exp\left[\frac{U_{s1}(\mathbf{x}_T, z=\Delta z)}{U_{\text{in}}}\right]\right|^2 & \text{Defocus}. \end{cases} \tag{4}$$

The combination of Eqs. (3) and (4) reveals the transport relationship of the 2D intensity in the axial direction for a 3D object under the Rytov approximation, and the realization of Eq. (4) is just the key concept of "transport-of-intensity" in this work. Unlike the TIE for 2D thin objects, the concept of "transport-of-intensity" here is the extension of the conventional one, and it is the typical phenomenon of volumetric intensity transport in the diffraction tomography for 3D objects. In addition, the concept originates from Fourier diffraction theorem, and the Rytov approximation is taken into account as well to make it more applicable for 3D diffraction tomographic imaging of biological samples.

B. Illumination Situations for TI-FPDT

For typical ODT based on holographic measurements, the complex amplitude of the total field $U(\mathbf{x_T})$ can be measured directly through an interferometric approach. As illustrated in Fig. 1(a), an off-axis hologram contains information about the total field, shifted by the oblique incident field in the Fourier domain. The total field can be extracted via the low-pass filtering of +1-order or −1-order frequency component of the hologram spectrum. After converting the obtained total field $U(\mathbf{x_T})$ to the first-order scattered field $U_{s1}(\mathbf{x_T})$ under the Born or Rytov approximations [Eq. (S1) or Eq. (S5)], the resultant 2D spectrum is projected onto the particular Ewald sphere in 3D Fourier space, according to the relation given by Eq. (2). By changing the incident illumination angle to enlarge the accessible object spectrum, a certain portion of $\hat{O}(\mathbf{u})$ can be retrieved, which will allow us to reconstruct the 3D RI distribution of samples.

For non-interferometric ODT based on intensity-only measurements, we cannot directly measure the complex amplitude of the total field since the inherent intensity recording leads to the loss of phase component. However, the phase component of the scattered field decisively contains the information about the RI distribution of samples. Therefore, the key to non-interferometric ODT implementation is the encoding of phase information into intensity images through modulations [38] (e.g., matched illumination or axial defocus) and the recovery of desired phase component using phase retrieval algorithms during the reconstruction process. This phase encoding process can be intuitively interpreted from the perspective of the PTF.

Considering the case of weak scattering and negligible absorption properties for the most biological samples [39], the detection intensity on the in-focus ($z=0$) and defocused ($z=\Delta z$) planes in Fourier space under flexible illumination angles can be stated as follows:

$$I(\mathbf{u}_T;\, z=0,\, \Delta z) = a_0^2\left[\delta(\mathbf{u}_T) + j H_P(\mathbf{u}_T;\, z=0,\, \Delta z)\Phi(\mathbf{u}_T)\right], \tag{5}$$

where a_0 is the mean value of amplitude in the in-focus plane and $\Phi(\mathbf{u}_T)$ corresponds to the Fourier transform of phase component $\phi(\mathbf{x}_T)$. $H_P(\mathbf{u}_T)$ is the PTF in the in-focus and defocused planes written in the following form [30,40]:

$$H_P(\mathbf{u}_T) = \begin{cases} P(\mathbf{u}_T - \mathbf{u}_{\text{in}T}) - P(\mathbf{u}_T + \mathbf{u}_{\text{in}T}) & z=0, \\ P(\mathbf{u}_T - \mathbf{u}_{\text{in}T})\exp\left\{j\frac{2\pi}{\lambda}\Delta z[\eta(\mathbf{u}_T - \mathbf{u}_{\text{in}T}) - \eta(\mathbf{u}_{\text{in}T})]\right\} & \\ -P(\mathbf{u}_T + \mathbf{u}_{\text{in}T})\exp\left\{j\frac{2\pi}{\lambda}\Delta z[\eta(\mathbf{u}_T + \mathbf{u}_{\text{in}T}) - \eta(\mathbf{u}_{\text{in}T})]\right\} & z=\Delta z, \end{cases} \tag{6}$$

where $P(\mathbf{u}_T)$ is the 2D circular pupil function with a radius of $\text{NA}_{\text{obj}}/\lambda$ ideally, and $\eta(\mathbf{u}_T) = \sqrt{n_m^2 - \lambda^2|\mathbf{u}_T|^2}$ denotes the axial spatial frequency for an aberration-free system.

Figure 1(b) exhibits the PTFs distribution under different illumination conditions and detection planes. The recorded raw intensity images and their corresponding spectra are shown in

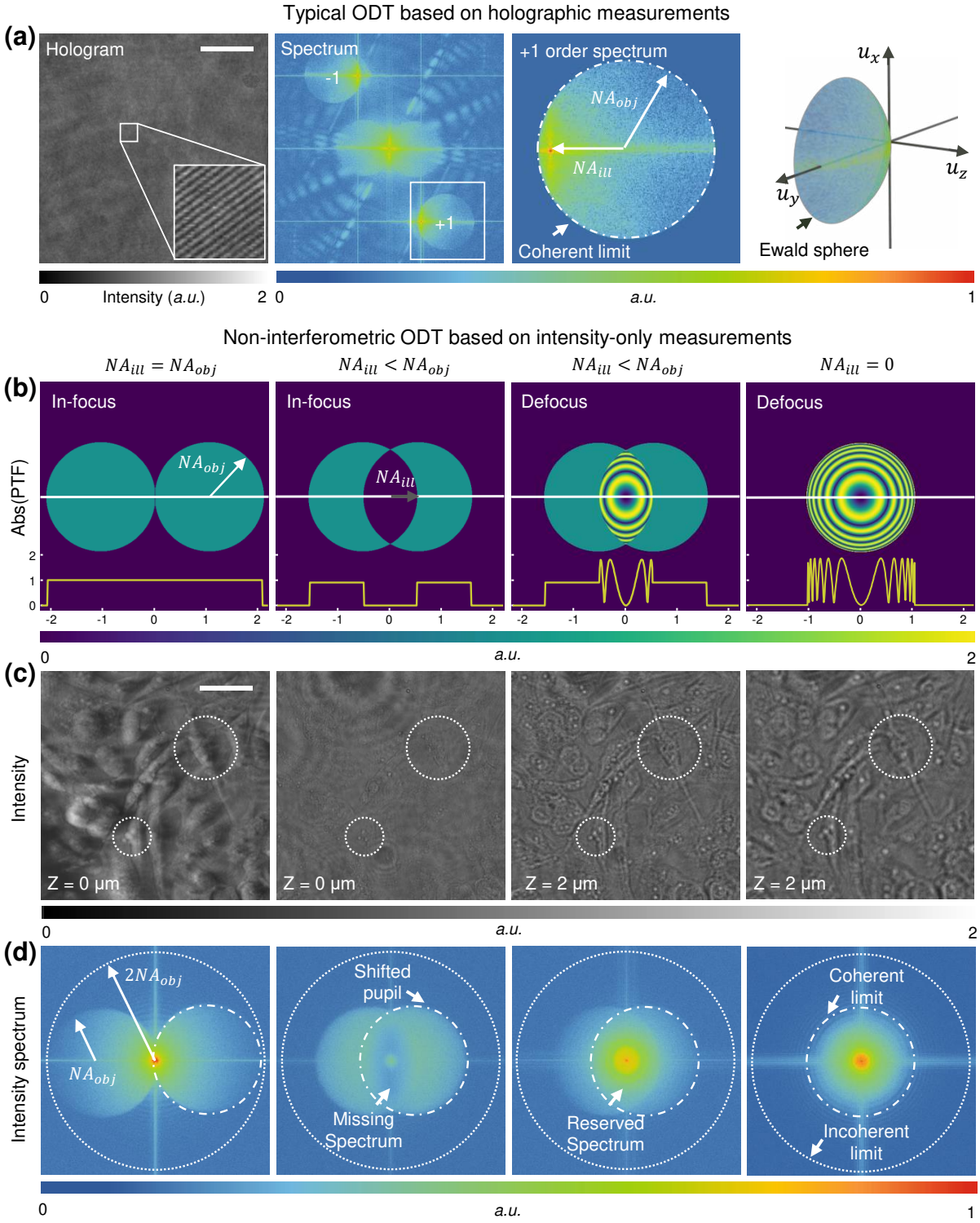

Fig. 1. Illustrate the principle of holographic diffraction tomography and understand the importance of illumination conditions for non-interferometric ODT from the perspective of the PTF. (a) Typical ODT implementation based on holographic measurements. (b) Absolute value distribution of the PTFs under different illumination conditions and at different focal planes. (c), (d) Intensity images captured in the four different situations and corresponding spectra. Scale bars, 10 μm.

Figs. 1(c) and 1(d). It can be found that, for a perfectly in-focus imaging system, the two anti-symmetrical (positive and negative) pupils of $H_P(\mathbf{u}_T; z = 0)$ are tangent to each other under matched illumination condition, suggesting the phase information within pupil function can be totally transferred to the intensity images. The intensity spectrum corresponding to this case has almost the same frequency support as the PTF. If the illumination angle is reduced, i.e., under the non-matched illumination condition, the two pupils are no longer completely tangential and cancel each other out in the low-frequency position. In this case, the low-frequency phase components (near zero frequency) cannot be transferred to the intensity images, and this issue is also validated

by the phenomenon of the missing low-frequency spectrum in the captured intensity image.

In addition to illumination modulation, TI-FPDT incorporates another more convenient way of encoding phase into the intensity image, which is to introduce an imaginary part into the transfer function through defocus modulation. Under arbitrary illumination conditions, the two pupils of $H_P(\mathbf{u}_T; z=\Delta z)$ in the defocused plane may overlap but will not completely cancel each other out. The absolute value distribution of the PTFs shown in Fig. 1(b) indicates that $H_P(\mathbf{u}_T; z=\Delta z)$ is always non-zero in the shifted pupil function (except for the zero-frequency since the zero-frequency of the PTF is meaningless). This means that the phase components in the accessible frequency domain, especially the low frequencies, can be totally transferred to the intensity images. Intuitively, Eq. (6) can be expressed along the direction of incident illumination spatial frequency $\mathbf{u}_{\mathrm{in}\,T}$ as

$$|H_P(\mathbf{u}_T)| = \begin{cases} 0 & z=0, \\ \left|\exp\left\{j\frac{2\pi}{\lambda}\Delta z[\eta(\mathbf{u}_T-\mathbf{u}_{\mathrm{in}\,T})-\eta(\mathbf{u}_{\mathrm{in}\,T})]\right\}\right. & \\ \left.-\exp\left\{j\frac{2\pi}{\lambda}\Delta z[\eta(\mathbf{u}_T+\mathbf{u}_{\mathrm{in}\,T})-\eta(\mathbf{u}_{\mathrm{in}\,T})]\right\}\right| & z=\Delta z, \end{cases} \tag{7}$$

for the case of low-frequency region within $0<|\mathbf{u}_T|<\mathrm{NA_{obj}}-\mathrm{NA_{ill}}$, and

$$|H_P(\mathbf{u}_T)| = \begin{cases} 1 & z=0, \\ 1 & z=\Delta z, \end{cases} \tag{8}$$

for the case of high-frequency region within $\mathrm{NA_{obj}}-\mathrm{NA_{ill}} \le |\mathbf{u}_T| \le \mathrm{NA_{obj}}+\mathrm{NA_{ill}}$. The line profiles corresponding to the four different situations are plotted in Fig. 1(b).

Thus, the phase components of the sample scattering can be totally transferred to the measured intensity images by combining ptychographic angular diversity with additional defocused intensity measurements, allowing TI-FPDT to retrieve RI tomograms without suffering from reconstruction quality deterioration

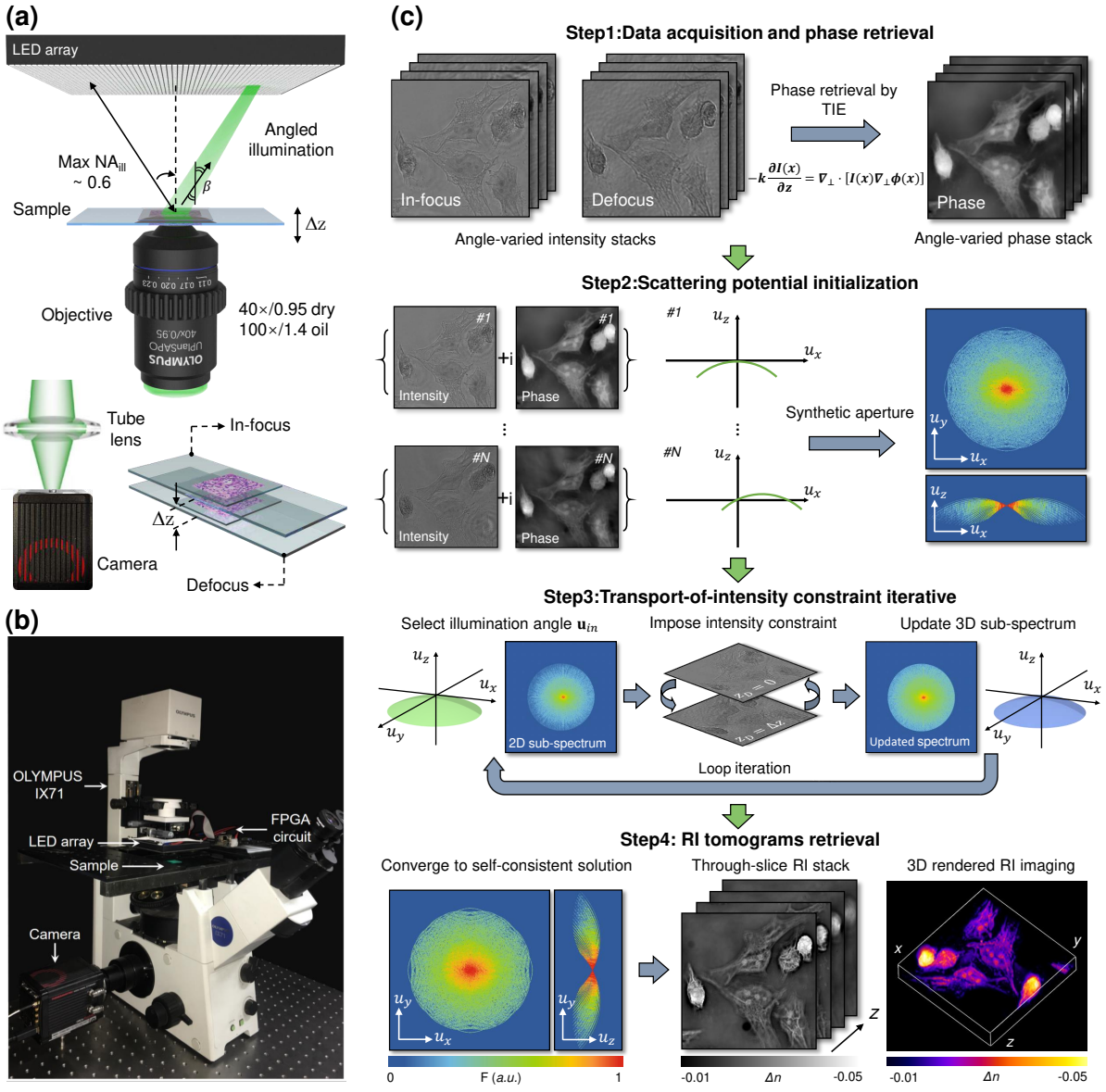

Fig. 2. Hardware implementation and working flow of TI-FPDT. (a) Setup of TI-FPDT system based on a commercial microscope equipped with a programmable LED array source. (b) Photograph of the TI-FPDT platform. (c) Flow chart of data processing in TI-FPDT for 3D RI reconstruction on the example of unstained HeLa cells.

and RI underestimation problems, even under the non-matched illumination condition.

C. Hardware Implementation

Due to the advantage of non-interferometric measurements, TI-FPDT can be easily implemented on a commercial inverted bright-field microscope (IX71, Olympus, Japan) assisted by programmable 23 × 23 LED array illumination, as shown in Figs. 2(a) and 2(b). The LED array with 2 mm pixel size, placed 30 mm away from the sample stage, provides quasi-monochromatic illumination with a center wavelength of 507 nm and spectral bandwidth of 20 nm. These LED elements are controlled to turn on sequentially by a field-programmable gate array (FPGA) unit (EP4CE10E22C8N, Intel, US), and the illumination beam passes through the sample from different directions. In order to achieve isotropic transverse resolution, 377 LED elements within the circular area in the array where the center of the circle coincides with the optical axis are selected, which provide angle-varied plane wave illuminations with available maximum illumination NA of 0.6. A CMOS camera (Hamamatsu ORCA-Flash 4.0 C13440) with a resolution of 2048 × 2048 and a pixel size of 6.5 μm is used to record the intensity information under detection objectives (40 × /0.95 UPLSAPO, Olympus or 100 × /1.4 Oil, UPLSAPO, Olympus), which is synchronized with the LED array by the same controller via two coaxial cables that provide the trigger and monitor the exposure status. Combining it with the axial movement synchronization, we can obtain two angle-varied intensity sets at two separate focus positions. Under the camera exposure rate of 5 Hz/2 Hz, a total of 754 full-frame (2048 × 2048) 16-bit images are captured within 2.52 min/6.29 min with dry/oil-immersion objectives, respectively. All the experimental data are processed by MATLAB software (MATLAB R2018a) on a computer workstation.

D. TI-FPDT Reconstruction Algorithm

Figure 2(c) illustrates the working flow of the TI-FPDT algorithm for 3D RI reconstruction, taking unstained HeLa cells as an example. The proposed TI-FPDT algorithm provides an iterative solver for the inverse scattering problem, which retrieves the 3D RI distribution of the sample based on the transport-of-intensity constraint iterative in the FPDT reconstruction framework. First, assisted by LED illumination and axial movement synchronization, two angle-varied intensity sets are acquired at two separate focus positions. By solving the TIE for each pair of intensity images (in-focus images and defocused images), the corresponding roughly 2D phase maps can be obtained at different illumination angles [see Step1 in Fig. 2(c)]. As shown in Step2, the first-order scattered field composed of in-focus intensity and the retrieved phase at each illumination angle is acquired under the Rytov approximation [9], and the initialized 3D scattering potential spectrum is filled with the spectra of the first-order scattered fields according to the Fourier diffraction theorem [19]. Due to the invoking of the finite difference approximation [32,41] and phase discrepancy [42,43] of the TIE solver, the nonlinear high-frequency components are partially missed in the process of phase retrieval; thus, the transport-of-intensity constraint iteration must be performed on the initial scattering potential to compensate for the nonlinear error for accurate 3D RI recovery.

In Step3, the 3D Ewald spectrum of an arbitrary illumination angle is projected to the 2D plane, and the intensity constraint is imposed on the 2D scattered field on the in-focus plane. Next, the updated scattered field is propagated to the defocused plane [Eq. (3)], and the defocused intensity information is likewise transferred to the first-order scattered field under the Rytov approximation in this iterative process of transport-of-intensity constraint [Eq. (4)]. After that, the updated complex scattered field on the defocused plane is then backpropagated to the in-focus plane, and we repeat the intensity constraint on the in-focus plane. Finally, the resultant 2D spectrum is mapped to the 3D spectrum of scattering potential, and we implement the loop iteration of Step3 again for another illumination angle. The iterative process is repeated for all illumination angles until the transport-of-intensity constraint iteration of TI-FPDT converges within all intensity images. As illustrated in Step4 of Fig. 2, the 3D inverse Fourier transform is applied to the convergent scattering potential spectrum, and the 3D RI distribution of the sample can, thus, be reconstructed.

As the advanced expansion of FPDT, the proposed TI-FPDT employs the combined modulation strategies (both illumination scanning and axial defocus) and enables the correct recovery of 3D RI distribution in the case of the non-matched illumination condition. The introduction of the defocused intensity image confers the ability of TI-FPDT to bypass the matched illumination barrier, and this advantage appears more obvious in the case of high-NA imaging.

E. Validation of TI-FPDT on Both Simulations and Experiments

Followed by the given hardware implementation and reconstruction algorithm for TI-FPDT, we simulate a pure phase microsphere as the test sample to validate its capability for quantitative 3D RI reconstruction, in which the optical parameters are the same as the polystyrene microsphere and imaging system in the experiment. The ideal microsphere with an 8 μm diameter and RI of 1.60 is immersed in the matched medium ($n_m = 1.58$). Angle-varied plane wave illuminations with a center wavelength of 507 nm pass through the sample sequentially, and we generate or measure 754 intensity images, each containing 200 × 200 pixels with a pixel size of 6.5 μm.

Since the maximum illumination NA 0.6 is smaller than the 40 × /0.95 objective NA, the traditional FPDT method cannot correctly recover the RI of the microsphere, and only the sharp edges (high-frequency detail) can be reconstructed, as displayed in Fig. 2(a). This phenomenon is extremely consistent with our predicted low-frequency RI loss due to the non-matched illumination condition. Besides, we further demonstrate the inability of the FPDT to achieve low-frequency RI recovery using a single intensity stack under the non-matched illumination condition, either for in-focus or defocused one in Section 2 of Supplement 1. The TI-FPDT algorithm without Step2, i.e., only the transport-of-intensity constraint iteration between in-focus and defocused intensity images, is also performed for RI reconstruction. The corresponding result suggests the ability of the proposed iterative strategy for low-frequency RI recovery of the microsphere, thanks to the low-frequency phase contrast provided by the additional defocused intensity images acquired at each illumination angle. However, the iterative process often exhibits slow convergence and

stagnation due to the significant difference between the initial zero values and the true RI to be solved.

After applying the complete TI-FPDT procedure, we can correctly recover the 3D RI distribution with several rounds of iteration. The indistinguishable differences between the results and the given true value corresponding to the finite identical illumination angles [Fig. 3(b)] demonstrate that the proposed technique can effectively achieve quantitative RI recovery and overcome the reconstruction quality deterioration and RI underestimation problems in conventional FPDT under the non-matched illumination condition. Experimental results obtained from three different reconstruction methods agree with the simulations and validate the main conclusions. Based on the experimental results of TI-FPDT, a post-processing algorithm based on the nonnegative constraint iterative is invoked to computationally fill the missing cone region to obtain a 3D RI reconstruction result that matches the theoretical RI value of 1.6 [Fig. 3(c)]. Both simulations and experiments of microspheres verify the quantitative reconstruction capability of the proposed TI-FPDT, which reconstructs the RI value close to the true value with a missing cone. The nonnegative constraint allows the final RI distribution to match the theoretical value, while the axial profile of the microsphere is also close to spherical [Fig. 3(c)]. In addition, the comparison of recovered through-slice RI stacks and the corresponding 3D rendered images using FPDT and TI-FPDT is animated in Visualization 1. Finally, the cross correlation coefficient between 3D RI tomograms and the true value for the three reconstruction methods during the iterative process, illustrated in Fig. 3(d), highlights the fast and stable convergence advantages of TI-FPDT.

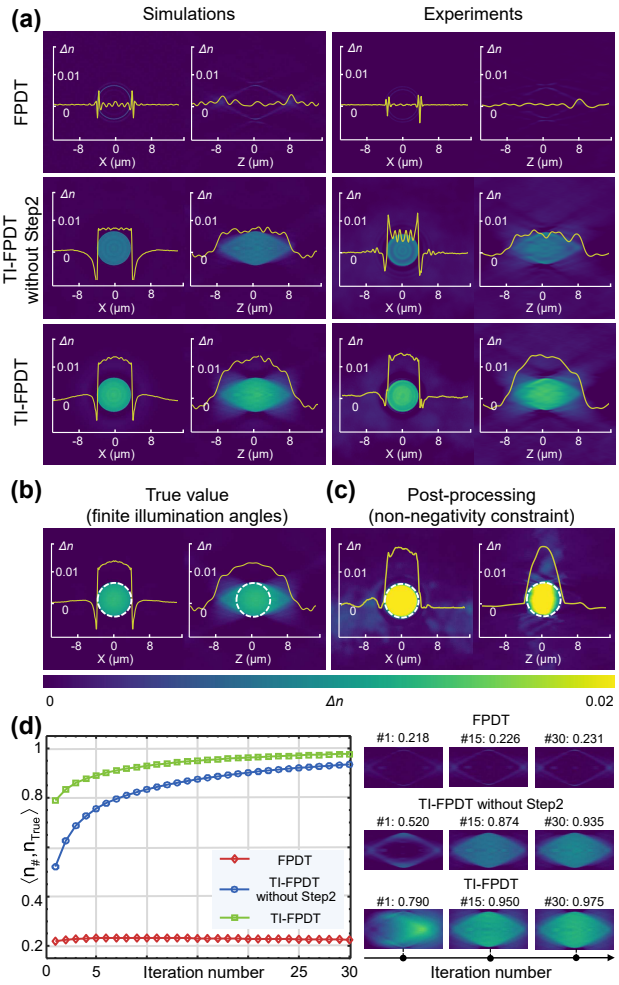

Fig. 3. Validation of TI-FPDT by 3D RI reconstruction of polystyrene microspheres in simulations and experiments. (a) Lateral and axial RI slices of reconstructed microspheres with 8 μm diameter via three different reconstruction methods in simulations and experiments, respectively. (b) True value of the simulated microsphere corresponding to the finite illumination angles. (c) Lateral and axial RI slices of reconstructed microspheres with nonnegativity iterative constraint based on the result of TI-FPDT in the experiment. (d) Cross correlation coefficient between 3D RI tomograms and true value for the three reconstruction methods during the iterative process, and cross correlation coefficient and axial RI slices of reconstructed tomograms corresponding to different iteration numbers (see also Visualization 1).

3. RESULT

A. Resolution Benchmarking of TI-FPDT with USAF Targets

In order to demonstrate the performance of the proposed method, we use United States Air Force (USAF) resolution targets to benchmark the resolution limit of TI-FPDT, and the 3D imaging resolution analysis and quantitative characterization are provided as well (Fig. 4). The absorption and phase resolution targets are considered as 3D objects horizontally placed on the sample stage of the microscope, for which the TI-FPDT is used to reconstruct the 3D absorption or RI distribution. Due to the inherent synthetic aperture process, the TI-FPDT technique expands the accessible 3D Fourier domain by sequentially illuminating a 3D object from various directions, thereby improving the lateral and axial resolution of the system. Note that the resolution limit of the TI-FPDT is determined by the highest accessible frequency of the scattering potential spectrum [6,34,44].

For the reconstruction of the absorption resolution target, the initial phase estimation in the TI-FPDT algorithm [Step1 and Step2 in Fig. 2(b)] is not required since there are no phase components to be recovered. The spectra of the recovered scattering potential absorption component are illustrated in Figs. 4(e1) and 4(e2). Employing the parameters of $NA_{ill} = 0.6$ and $NA_{obj} = 0.95$ as well the resolution definition formula

$$\Delta_{x,y} = \frac{\lambda}{NA_{ill} + NA_{obj}}, \quad \Delta_z = \frac{\lambda}{1 - \sqrt{1 - NA_{ill}^2}}, \tag{9}$$

it can be calculated that the theoretical full-width lateral resolution is 327 nm and axial resolution is 2.54 μm, respectively. Figures 4(b) and 4(c) both with the corresponding line profiles shown in Fig. 4(d) confirm the enhanced lateral resolution from 488 nm (Group 11, Element 1) of coherent microscopy imaging to 346 nm (Group 11, Element 4) of synthetic aperture microscopy imaging, which is well-consistent with the theoretical resolution limit. Additional cross sectional reconstruction and 3D volume-rendered imaging are shown in Visualization 2.

As shown in Fig. 4(g1), the in-focus intensity image captured under coherent illumination exhibits extremely weak contrast because the phase resolution target is a transparent sample. Simple defocus modulation allows phase information to be transferred into intensity information, improving image contrast [Fig. 4(g2)]. The traditional FPDT algorithm, which uses only the in-focus intensity stack for reconstruction, cannot correctly recover the RI distribution because of the lack of low-frequency phase (RI) information in the in-focus intensity images under the non-matched

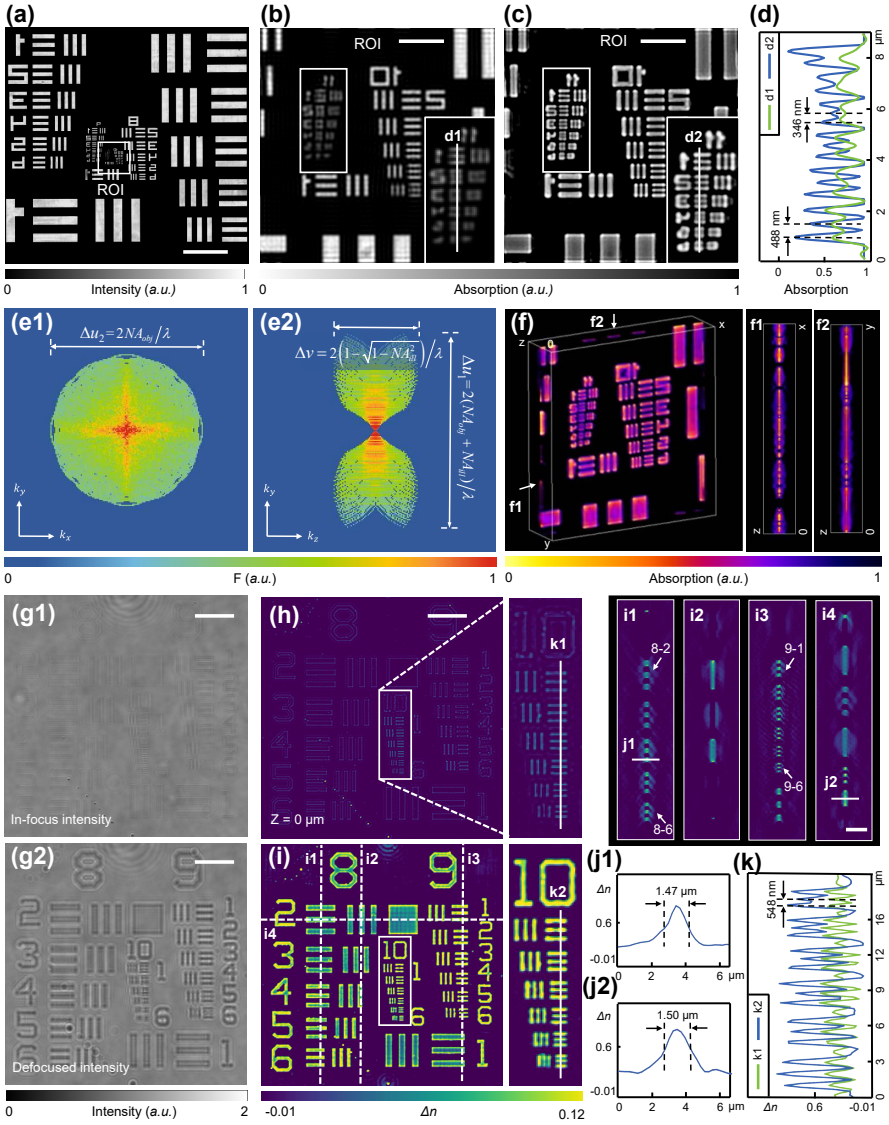

Fig. 4. Resolution benchmarking of TI-FPDT with both absorption and phase resolution target under 0.95 NA objective. (a) The intensity image of the absorption resolution target at vertical coherent illumination. (b) Enlarged raw image corresponding to the ROI. (c) High-resolution recovery result at in-focus plane using the TI-FPDT algorithm. (d) The corresponding line profiles in (b) and (c) are shown to compare the imaging resolution. (e1), (e2) Lateral and axial sections of the recovered high-resolution 3D absorption spectrum. (f) Volume-rendered imaging of the reconstructed result (see also Visualization 2). (g1), (g2) In-focus and defocused intensity images of phase resolution target at vertical coherent illumination. (h), (i) Reconstructed RI slices at the in-focus plane using FPDT and TI-FPDT. (i1)–(i4) Multiple axial RI sections of reconstructed phase resolution target. (j1), (j2) The cross section RI profile plots are shown to indicate axial resolution. (k) RI line profiles corresponding to the markers in (h) and (j) present the quantitative RI recovery (see also Visualization 3). Scale bars, (a) 40 μm; (b), (c) 5 μm; (g)–(i) 10 μm; (i1)–(i4) 5 μm.

illumination condition. The corresponding result is shown in Fig. 4(h).

Thanks to the phase contrast contained in the defocused intensity images, the proposed TI-FPDT algorithm successfully recovers the RI of the sample from two intensity sets in an iterative manner. The reconstructed RI slice at 0 μm z plane and multiple axial sections are shown in Fig. 4(i), presenting clearer RI results compared to Fig. 4(h). The slight depression of RI values originated from the missing cone of the 3D scattering potential spectrum at the limited illumination angle. Quantitative characterizations displayed in Figs. 4(j)–4(k) demonstrate that TI-FPDT achieves systematic theoretical resolution while ensuring RI recovery. Since the theoretical lateral resolution of the TI-FPDT system is about 327 nm far beyond the minimum bar in phase target, we can only clearly see element 6 of group 10. The missing cone issue in the direction near the low zero-frequency area results in the actual axial resolution being slightly lower than the theoretical resolution [34,45]. The width at half-maxima of line profiles in Figs. 4(j1) and 4(j2) confirms the half-width axial resolution of about 1.5 μm, in accordance with the theoretical prediction of 1.27 μm within the error allowed. Finally, additional through-slice RI stacks and 3D volume renderings are shown in Visualization 3.

B. Tomographic Imaging of Unstained HeLa Cells

To illustrate the biological applications of TI-FPDT, we first image unstained HeLa cells and have achieved high-resolution RI tomography. Figures 5(a) and 5(b) show the reconstructed RI maps using

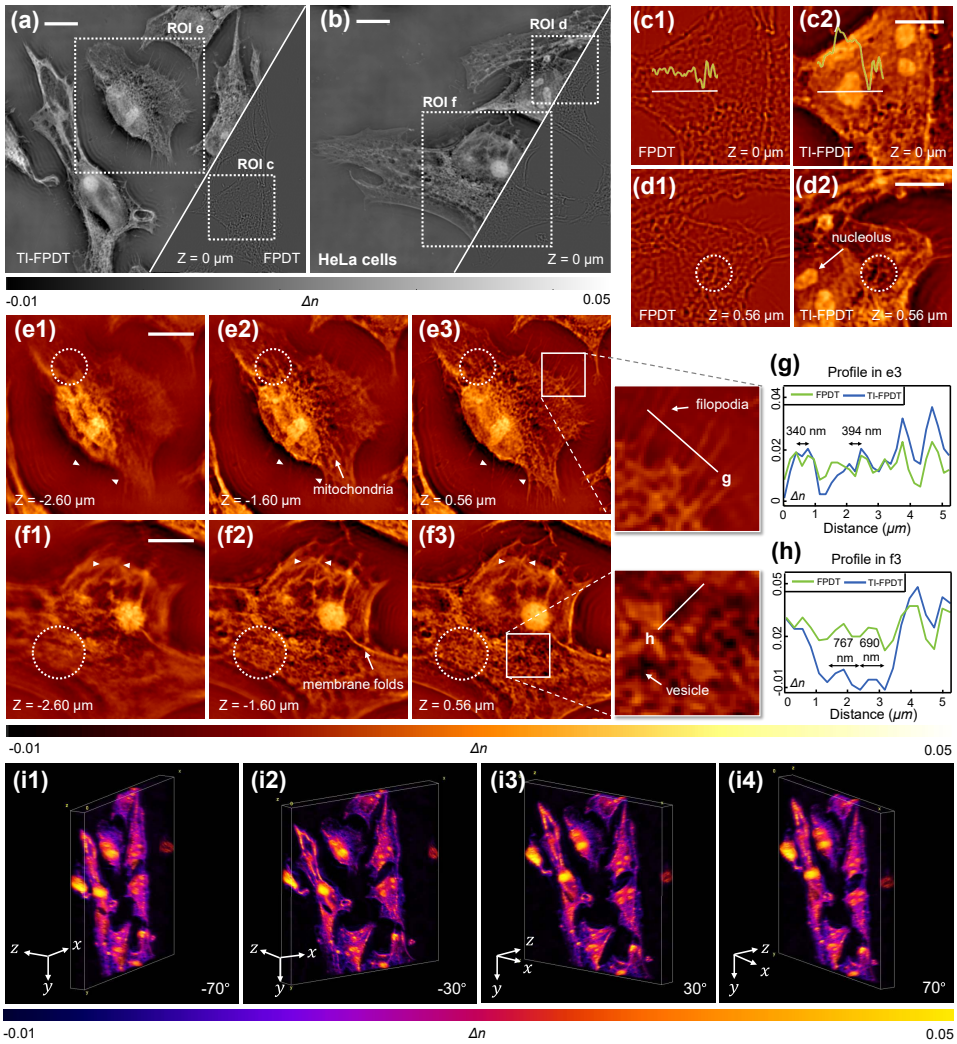

Fig. 5. RI reconstruction of unstained HeLa cells imaged with 40 × 0.95 NA objective. (a), (b) RI reconstruction of HeLa cells using TI-FPDT and FPDT at 0 μm z plane for two different subregions in 40× FOV. (c1), (c2), (d1), (d2) Two RI slices recovered using FPDT and TI-FPDT corresponding to rectangular subregions in (a) and (b). (e), (f) RI distribution of HeLa cells at multiple z planes corresponds to two square subregions. (g), (h) RI line profiles across subcellular structures quantify the lateral resolution and RI values. (i1)–(i4) 3D volume-rendered views of reconstructed HeLa cells under different perspectives. Scale bars, (a), (b) 10 μm; (c), (d) 5 μm; (e), (f) 10 μm.

TI-FPDT at 0 μm z plane for two different subregions in 40× field of view (FOV), supplemented by the reconstruction results using FPDT as controls. The magnified RI distributions corresponding to the rectangular subregions together with the line profiles across nucleoli displayed in Figs. 5(c1)–5(d2) highlight the differences in the low-frequency components of the reconstruction results under two different algorithms. The comparisons suggest the proposed method is very effective for recovering the RI of biological cells, which overcomes the issue of RI underestimation caused by the non-matched illumination condition and achieves more accurate RI recovery.

The tomograms of two regions of interest at different axial depths show high-resolution filopodia and other subcellular features, including cellular membrane folds, cell boundaries, nucleoli, mitochondria, and black vesicles [see Figs. 5(e)–5(f)]. Besides, we zoomed in on two square subregions in Figs. 5(e3) and 5(f3) to highlight the fine structure of filopodia, vesicles, and mitochondria. Line profiles across subcellular structures quantify the RI of organelles and confirm near-diffraction-limited lateral resolution of 327 nm on RI imaging, as shown in Figs. 5(g) and 5(h). 3D volume-rendered views of reconstructed HeLa cells under four different perspectives are displayed in Figs. 5(i1)–5(i4) to visually represent the 3D structure and distribution of the sample. More information about recovered through-slice RI stack and 3D volume rendering of other HeLa cells is animated in Visualization 4.

In addition, we compared the reconstruction results under the Born and Rytov approximation using HeLa cells to understand how the accuracy of the forward scattering model affects the reverse reconstruction (see Section 3 in Supplement 1 for detailed analysis). Finally, the recovered RI tomograms using the TI-FPDT algorithm with and without iteration process are also compared to suggest the importance of the transport-of-intensity constraint iteration for compensating inaccuracies originating from TIE solvers and refining 3D RI recovery (see Section 4 in Supplement 1 for detailed analysis). All results reveal that we can clearly image the details of 3D structures of biological samples throughout the entire

volume and quantify the RI at the subcellular level by applying TI-FPDT.

C. 3D RI Tomography on C2C12 Cell

We also apply our method to 3D RI reconstruction of murine skeletal myoblasts C2C12 cells with 100 × /1.4 NA oil-immersion objective to verify the ability of TI-FPDT for application in higher NA microscopic systems. A full FOV in-focus intensity image of C2C12 cells collected under vertical illumination is illustrated in Fig. 6(a). With the aid of TI-FPDT and endogenous contrast agent, reconstructed high-resolution and high-contrast RI tomograms at multiple planes and directions are shown in Figs. 6(b) and 6(c).

In addition, we select a single cell region and show its intensity, absorption, and RI distribution at 0 μm z plane [Figs. 6(d1)–6(d3)]. Three tomograms at different axial depths clearly display subcellular structures inside the C2C12 cell, such as tiny bright lipid droplets [Fig. 6(e1)], large bright nucleoli [Fig. 6(e2)], and black vesicles [Fig. 6(e3)]. Line profiles quantify the RI of organelles, suggesting that the RI values of lipid droplets are higher compared to the average index of cytoplasm. Also, line profiles across the boundary of the cytomembrane verify near-diffraction-limited full-width lateral resolution of 254 nm in 100 × /1.4 NA oil-immersion objective microscopy. Besides, the projections of 3D RI rendering results in $x-y$, $y-z$, and $x-z$ directions, as shown in Fig. 6(h), help us to visualize the overall structure and morphology of a single C2C12 cell. The experimental results basically demonstrate the ability of the TI-FPDT algorithm to be applied in higher NA imaging systems to distinguish finer subcellular structures. Due to the advantage of defying the matched illumination condition, we only need to switch the higher NA objective without controlling the illumination NA to precisely match the objective NA. Applying TI-FPDT allows us to easily operate in tomographic imaging experiments with different objectives for meeting the requirements of different imaging FOV and imaging resolutions.

4. CONCLUSION AND DISCUSSION

In summary, we have presented TI-FPDT, a new non-interferometric ODT technique for the reconstruction of 3D complex RI distribution, and this novel approach effectively addresses the challenging issue posed by the matched illumination condition by combining ptychographic angular diversity with additional "transport of intensity" measurements. Thanks to the enhancement of low-frequency phase contrast introduced by the additional defocused intensity image under oblique illumination, the proposed TI-FPDT circumvents the stringent requirement on the illumination NA imposed by the matched illumination condition, endowing the capability to overcome the reconstruction quality deterioration and RI underestimation problems in conventional FPDT. As a non-interferometric ODT without the requirement of the matched illumination condition, a classic commercial bright-field microscope tends to be upgraded to a simple and reliable 3D RI tomographic microscope by replacing the light source with a programmable LED array. Overall, TI-FPDT achieves high-resolution and high-quality 3D RI imaging and gathers the advantages of non-interferometric ODT including speckle-free illumination, easy hardware implementation, optical path stability, and synthetic aperture resolution, which make it

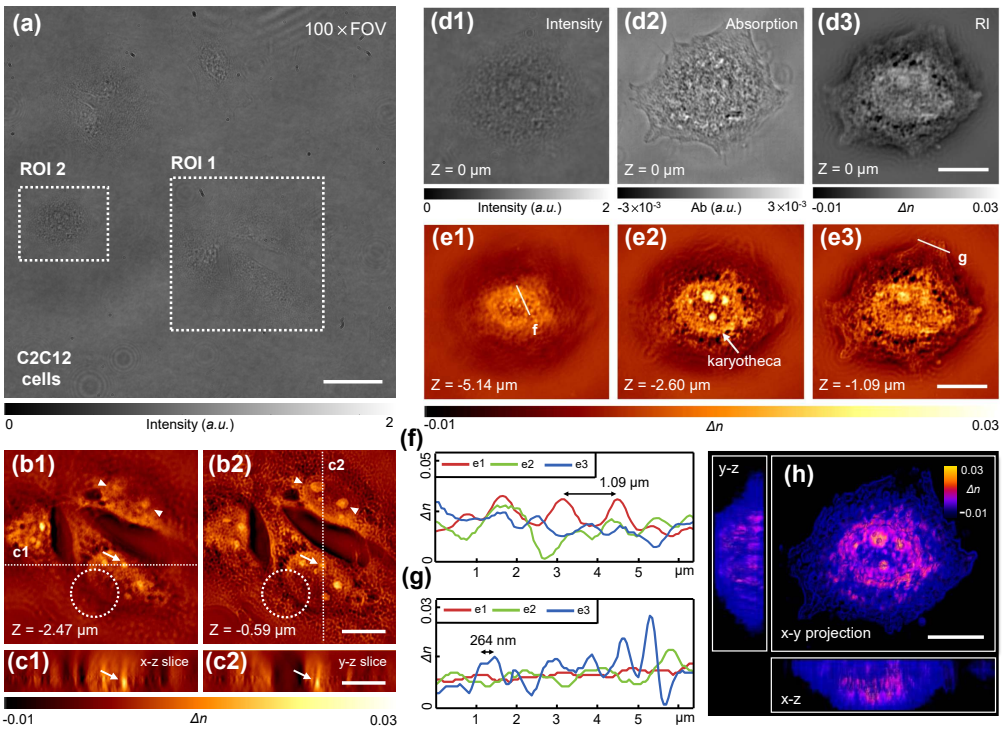

Fig. 6. 3D RI tomography on unstained C2C12 cells imaged with 100 × /1.4 NA objective. (a) Full FOV intensity image of C2C12 cells collected under vertical illumination. (b1), (b2) Reconstructed RI distribution of multiple cells at two z planes from ROI 1. (c1), (c2) RI slices along the $x-z$ and $y-z$ directions. (d1)–(d3) Corresponding intensity, reconstructed absorption, and RI of single cell at 0 μm z plane from ROI 2. (e1)–(e3) Reconstructed RI distribution of C2C12 cells at multiple z planes. (f)–(g) RI line profiles across subcellular structures at multiple z planes quantify the lateral resolution and RI values. (h) Projections of 3D RI rendering results in $x-y$, $y-z$, and $x-z$ directions. Scale bars, (a) 20 μm; (b)–(e) 10 μm.

attractive as a non-invasive 3D imaging tool for various biological and medical applications. Experimentally, we first demonstrated the quantitative properties of TI-FPDT by simulating a pure phase microsphere and confirmed them by imaging standard polystyrene beads. The 3D tomographic results of USAF targets and biological cells further indicated the full-width lateral imaging resolution of 327 nm and 254 nm with dry/oil-immersion objectives, respectively. Finally, high-resolution tomographic RI characterizations of unstained HeLa and C2C12 cells revealed the subcellular organelle structures, demonstrating the applicability of TI-FPDT for 3D label-free imaging of biological samples.

However, as a preliminary and exploratory technique, TI-FPDT has not yet been fully investigated and optimized in terms of acquisition speed and imaging performance. The proposed tomographic technique still relies on the first-order Rytov approximation, whose validity depends on the RI gradient within the sample; therefore, it does not work well in the case of multi-layer or multiple scattering [46–48]. Moreover, there is still data redundancy in the angle-varied intensity stack due to dense sequential illumination sampling of LED arrays, and the amount of data can be reduced by combining the sparse annular illumination strategy proposed in previous works [49,50]. Besides, the acquisition speed is mainly limited by the z axis movement via the mechanical drive, and the optical devices, including spatial light modulator [51,52] and electrically tunable lens [53,54], can be used to accelerate the acquisition speed of TI-FPDT. Finally, recently emerged learning-based 3D tomographic approaches will be invoked to fully parameterize the missing cone artifact and unknown experimental variables, such as optical aberrations and slight misalignment of LED, and to further optimize imaging performance [55–58]. By addressing the above-mentioned drawbacks, TI-FPDT is expected to fulfill expectations for high-quality 3D volumetric imaging and real-time dynamic monitoring of cell morphology in future work.

Funding. China Postdoctoral Science Foundation (2022M711644); Key National Industrial Technology Cooperation Foundation of Jiangsu Province (BZ2022039); Biomedical Competition Foundation of Jiangsu Province (BE2022847); Open Research Fund of Jiangsu Key Laboratory of Spectral Imaging & Intelligent Sense (JSGP202105, JSGP202201); Fundamental Research Funds for the Central Universities (30920032101); Youth Foundation of Jiangsu Province (BK20190445, BK20210338); Leading Technology of Jiangsu Basic Research Plan (BK20192003); National Natural Science Foundation of China (61905115, 62105151, 62175109, U21B2033); National Major Scientific Instrument Development Project (62227818).

Disclosures. The authors declare no conflicts of interest.

Data availability. The data that support the findings of this study are available from the corresponding author upon reasonable request.

Supplemental document. See Supplement 1 for supporting content.

[†]These authors contributed equally to this paper.

REFERENCES

1. Y. Park, C. Depeursinge, and G. Popescu, "Quantitative phase imaging in biomedicine," Nat. Photonics **12**, 578–589 (2018).
2. J. Yoon, Y. Jo, M.-h. Kim, K. Kim, S. Lee, S.-J. Kang, and Y. Park, "Identification of non-activated lymphocytes using three-dimensional refractive index tomography and machine learning," Sci. Rep. **7**, 6654 (2017).
3. K. L. Cooper, S. Oh, Y. Sung, R. R. Dasari, M. W. Kirschner, and C. J. Tabin, "Multiple phases of chondrocyte enlargement underlie differences in skeletal proportions," Nature **495**, 375–378 (2013).
4. S. Kwon, Y. Lee, Y. Jung, J. H. Kim, B. Baek, B. Lim, J. Lee, I. Kim, and J. Lee, "Mitochondria-targeting indolizino[3, 2-*c*]quinolines as novel class of photosensitizers for photodynamic anticancer activity," Eur. J. Med. Chem. **148**, 116–127 (2018).
5. S. Y. Lee, H. J. Park, C. Best-Popescu, S. Jang, and Y. K. Park, "The effects of ethanol on the morphological and biochemical properties of individual human red blood cells," PLoS One **10**, e0145327 (2015).
6. K. Kim, J. Yoon, S. Shin, S. Lee, S.-A. Yang, and Y. Park, "Optical diffraction tomography techniques for the study of cell pathophysiology," J. Biomed. Photon. Eng. **2**, 020201 (2016).
7. W. Choi, C. Fang-Yen, K. Badizadegan, S. Oh, N. Lue, R. R. Dasari, and M. S. Feld, "Tomographic phase microscopy," Nat. Methods **4**, 717–719 (2007).
8. Y. Cotte, F. Toy, P. Jourdain, N. Pavillon, D. Boss, P. Magistretti, P. Marquet, and C. Depeursinge, "Marker-free phase nanoscopy," Nat. Photonics **7**, 113–117 (2013).
9. Y. Sung, W. Choi, C. Fang-Yen, K. Badizadegan, R. R. Dasari, and M. S. Feld, "Optical diffraction tomography for high resolution live cell imaging," Opt. Express **17**, 266–277 (2009).
10. F. Merola, P. Memmolo, L. Miccio, R. Savoia, M. Mugnano, A. Fontana, G. D'ippolito, A. Sardo, A. Iolascon, A. Gambale, and P. Ferraro, "Tomographic flow cytometry by digital holography," Light Sci. Appl. **6**, e16241 (2017).
11. A. Kuś, M. Dudek, B. Kemper, M. Kujawińska, and A. Vollmer, "Tomographic phase microscopy of living three-dimensional cell cultures," J. Biomed. Opt. **19**, 046009 (2014).
12. M. Lee, K. Kim, J. Oh, and Y. Park, "Isotropically resolved label-free tomographic imaging based on tomographic moulds for optical trapping," Light Sci. Appl. **10**, 102 (2021).
13. P. Marquet, B. Rappaz, P. J. Magistretti, E. Cuche, Y. Emery, T. Colomb, and C. Depeursinge, "Digital holographic microscopy: a noninvasive contrast imaging technique allowing quantitative visualization of living cells with subwavelength axial accuracy," Opt. Lett. **30**, 468–470 (2005).
14. B. Kemper and G. Von Bally, "Digital holographic microscopy for live cell applications and technical inspection," Appl. Opt. **47**, A52–A61 (2008).
15. T. M. Buzug, "Computed tomography," in *Springer Handbook of Medical Technology* (Springer, 2011), pp. 311–342.
16. V. Mico, Z. Zalevsky, P. García-Martnez, and J. García, "Synthetic aperture superresolution with multiple off-axis holograms," J. Opt. Soc. Am. A **23**, 3162–3170 (2006).
17. C. Zheng, D. Jin, Y. He, H. Lin, J. Hu, Z. Yaqoob, P. T. So, and R. Zhou, "High spatial and temporal resolution synthetic aperture phase microscopy," Adv. Photon. **2**, 065002 (2020).
18. J. Park, D. J. Brady, G. Zheng, L. Tian, and L. Gao, "Review of bio-optical imaging systems with a high space-bandwidth product," Adv. Photon. **3**, 044001 (2021).
19. E. Wolf, "Three-dimensional structure determination of semi-transparent objects from holographic data," Opt. Commun. **1**, 153–156 (1969).
20. A. Devaney, "Inverse-scattering theory within the Rytov approximation," Opt. Lett. **6**, 374–376 (1981).
21. V. Lauer, "New approach to optical diffraction tomography yielding a vector equation of diffraction tomography and a novel tomographic microscope," J. Microsc. **205**, 165–176 (2002).
22. P. Ferraro, A. Wax, and Z. Zalevsky, *Coherent Light Microscopy: Imaging and Quantitative Phase Analysis* (Springer, 2011), Vol. **46**.
23. R. Ling, W. Tahir, H.-Y. Lin, H. Lee, and L. Tian, "High-throughput intensity diffraction tomography with a computational microscope," Biomed. Opt. Express **9**, 2130–2141 (2018).
24. J. Li, A. C. Matlock, Y. Li, Q. Chen, C. Zuo, and L. Tian, "High-speed *in vitro* intensity diffraction tomography," Adv. Photon. **1**, 066004 (2019).
25. C. Zuo, J. Sun, J. Li, A. Asundi, and Q. Chen, "Wide-field high-resolution 3D microscopy with Fourier ptychographic diffraction tomography," Opt. Lasers Eng. **128**, 106003 (2020).
26. R. Horstmeyer, J. Chung, X. Ou, G. Zheng, and C. Yang, "Diffraction tomography with Fourier ptychography," Optica **3**, 827–835 (2016).
27. L. Tian and L. Waller, "3D intensity and phase imaging from light field measurements in an LED array microscope," Optica **2**, 104–111 (2015).
28. Y. Baek and Y. Park, "Intensity-based holographic imaging via space-domain Kramers–Kronig relations," Nat. Photonics **15**, 354–360 (2021).
29. M. Chen, D. Ren, H.-Y. Liu, S. Chowdhury, and L. Waller, "Multi-layer Born multiple-scattering model for 3D phase microscopy," Optica **7**, 394–403 (2020).

30. J. Sun, C. Zuo, J. Zhang, Y. Fan, and Q. Chen, "High-speed Fourier ptychographic microscopy based on programmable annular illuminations," Sci. Rep. **8**, 7669 (2018).
31. J. Li, N. Zhou, J. Sun, S. Zhou, Z. Bai, L. Lu, Q. Chen, and C. Zuo, "Transport of intensity diffraction tomography with non-interferometric synthetic aperture for three-dimensional label-free microscopy," Light Sci. Appl. **11**, 154 (2022).
32. L. Waller, L. Tian, and G. Barbastathis, "Transport of intensity phase-amplitude imaging with higher order intensity derivatives," Opt. Express **18**, 12552–12561 (2010).
33. G. Zheng, R. Horstmeyer, and C. Yang, "Wide-field, high-resolution Fourier ptychographic microscopy," Nat. Photonics **7**, 739–745 (2013).
34. N. Streibl, "Three-dimensional imaging by a microscope," J. Opt. Soc. Am. A **2**, 121–127 (1985).
35. J. Li, Q. Chen, J. Sun, J. Zhang, J. Ding, and C. Zuo, "Three-dimensional tomographic microscopy technique with multi-frequency combination with partially coherent illuminations," Biomed. Opt. Express **9**, 2526–2542 (2018).
36. P. M. Morse and H. Feshbach, "Methods of theoretical physics," Am. J. Phys. **22**, 410–413 (1954).
37. J. M. Soto, J. A. Rodrigo, and T. Alieva, "Optical diffraction tomography with fully and partially coherent illumination in high numerical aperture label-free microscopy," Appl. Opt. **57**, A205–A214 (2018).
38. Y. Fan, J. Li, L. Lu, J. Sun, Y. Hu, J. Zhang, Z. Li, Q. Shen, B. Wang, R. Zhang, Q. Chen, and C. Zuo, "Smart computational light microscopes (SCLMs) of smart computational imaging laboratory (SCILab)," PhotoniX **2**, 1–64 (2021).
39. J. Sun, Q. Chen, J. Zhang, Y. Fan, and C. Zuo, "Single-shot quantitative phase microscopy based on color-multiplexed Fourier ptychography," Opt. Lett. **43**, 3365–3368 (2018).
40. C. Zuo, J. Sun, J. Li, J. Zhang, A. Asundi, and Q. Chen, "High-resolution transport-of-intensity quantitative phase microscopy with annular illumination," Sci. Rep. **7**, 7654 (2017).
41. C. Zuo, Q. Chen, Y. Yu, and A. Asundi, "Transport-of-intensity phase imaging using Savitzky-Golay differentiation filter–theory and applications," Opt. Express **21**, 5346–5362 (2013).
42. A. Shanker, L. Tian, M. Sczyrba, B. Connolly, A. Neureuther, and L. Waller, "Transport of intensity phase imaging in the presence of curl effects induced by strongly absorbing photomasks," Appl. Opt. **53**, J1–J6 (2014).
43. C. Zuo, Q. Chen, L. Huang, and A. Asundi, "Phase discrepancy analysis and compensation for fast Fourier transform based solution of the transport of intensity equation," Opt. Express **22**, 17172–17186 (2014).
44. O. Haeberlé, K. Belkebir, H. Giovaninni, and A. Sentenac, "Tomographic diffractive microscopy: basics, techniques and perspectives," J. Mod. Opt. **57**, 686–699 (2010).
45. S. S. Kou and C. J. Sheppard, "Imaging in digital holographic microscopy," Opt. Express **15**, 13640–13648 (2007).
46. U. S. Kamilov, I. N. Papadopoulos, M. H. Shoreh, A. Goy, C. Vonesch, M. Unser, and D. Psaltis, "Learning approach to optical tomography," Optica **2**, 517–522 (2015).
47. S. Chowdhury, M. Chen, R. Eckert, D. Ren, F. Wu, N. Repina, and L. Waller, "High-resolution 3D refractive index microscopy of multiple-scattering samples from intensity images," Optica **6**, 1211–1219 (2019).
48. M. Lee, H. Hugonnet, and Y. Park, "Inverse problem solver for multiple light scattering using modified Born series," Optica **9**, 177–182 (2022).
49. K. Kim, K. S. Kim, H. Park, J. C. Ye, and Y. Park, "Real-time visualization of 3-D dynamic microscopic objects using optical diffraction tomography," Opt. Express **21**, 32269–32278 (2013).
50. S. Zhou, J. Li, J. Sun, N. Zhou, Q. Chen, and C. Zuo, "Accelerated Fourier ptychographic diffraction tomography with sparse annular LED illuminations," J. Biophoton. **15**, e202100272 (2022).
51. C. Zuo, Q. Chen, W. Qu, and A. Asundi, "Noninterferometric single-shot quantitative phase microscopy," Opt. Lett. **38**, 3538–3541 (2013).
52. Z. Wang, L. Millet, M. Mir, H. Ding, S. Unarunotai, J. Rogers, M. U. Gillette, and G. Popescu, "Spatial light interference microscopy (SLIM)," Opt. Express **19**, 1016–1026 (2011).
53. C. Zuo, Q. Chen, W. Qu, and A. Asundi, "High-speed transport-of-intensity phase microscopy with an electrically tunable lens," Opt. Express **21**, 24060–24075 (2013).
54. J. A. Rodrigo, J. M. Soto, and T. Alieva, "Fast label-free microscopy technique for 3D dynamic quantitative imaging of living cells," Biomed. Opt. Express **8**, 5507–5517 (2017).
55. S. Jiang, K. Guo, J. Liao, and G. Zheng, "Solving Fourier ptychographic imaging problems via neural network modeling and tensorflow," Biomed. Opt. Express **9**, 3306–3319 (2018).
56. Y. Rivenson, Y. Zhang, H. Günaydn, D. Teng, and A. Ozcan, "Phase recovery and holographic image reconstruction using deep learning in neural networks," Light Sci. Appl. **7**, 17141 (2018).
57. Y. Xue, S. Cheng, Y. Li, and L. Tian, "Reliable deep-learning-based phase imaging with uncertainty quantification," Optica **6**, 618–629 (2019).
58. G. Barbastathis, A. Ozcan, and G. Situ, "On the use of deep learning for computational imaging," Optica **6**, 921–943 (2019).